

2010

Characterization of Evaporation and Boiling from Sintered Powder Wicks Fed by Capillary Action

J. A. Weibel

Purdue University - Main Campus

S. V. Garimella

Purdue University - Main Campus, sureshg@purdue.edu

M. T. North

Thermacore, Inc.

Follow this and additional works at: <http://docs.lib.purdue.edu/coolingpubs>

Weibel, J. A.; Garimella, S. V.; and North, M. T., "Characterization of Evaporation and Boiling from Sintered Powder Wicks Fed by Capillary Action" (2010). *CTRC Research Publications*. Paper 139.
<http://dx.doi.org/10.1016/j.ijheatmasstransfer.2010.05.043>

This document has been made available through Purdue e-Pubs, a service of the Purdue University Libraries. Please contact epubs@purdue.edu for additional information.



Characterization of evaporation and boiling from sintered powder wicks fed by capillary action

Justin A. Weibel^a, Suresh V. Garimella^{a,*}, Mark T. North^b

^aSchool of Mechanical Engineering and Birck Nanotechnology Center, Purdue University, 585 Purdue Mall, West Lafayette, IN 47907, USA

^bThermacore, Inc., 780 Eden Road, Lancaster, PA 17601, USA

ARTICLE INFO

Article history:

Received 8 February 2010

Received in revised form 12 May 2010

Accepted 12 May 2010

Available online 11 June 2010

Keywords:

Evaporation
Boiling
Thermal resistance
Heat pipe
Vapor chamber
Sintered powder wick
Microstructured surfaces

ABSTRACT

The thermal resistance to heat transfer into the evaporator section of heat pipes and vapor chambers plays a dominant role in governing their overall performance. It is therefore critical to quantify this resistance for commonly used sintered copper powder wick surfaces, both under evaporation and boiling conditions. The objective of the current study is to measure the dependence of thermal resistance on the thickness and particle size of such surfaces. A novel test facility is developed which feeds the test fluid, water, to the wick by capillary action. This simulates the feeding mechanism within an actual heat pipe, referred to as wicked evaporation or boiling. Experiments with multiple samples, with thicknesses ranging from 600 to 1200 μm and particle sizes from 45 to 355 μm , demonstrate that for a given wick thickness, an optimum particle size exists which maximizes the boiling heat transfer coefficient. The tests also show that monoporously sintered wicks are able to support local heat fluxes of greater than 500 W cm^{-2} without the occurrence of dryout. Additionally, in situ visualization of the wick surfaces during evaporation and boiling allows the thermal performance to be correlated with the observed regimes. It is seen that nucleate boiling from the wick substrate leads to substantially increased performance as compared to evaporation from the liquid free surface at the top of the wick layer. The sharp reduction in overall thermal resistance upon transition to a boiling regime is primarily attributable to the conductive resistance through the saturated wick material being bypassed.

© 2010 Elsevier Ltd. All rights reserved.

1. Introduction

Heat pipes and vapor chambers are widely employed in electronics cooling and other applications which demand efficient transport or spreading of heat from a localized source of high heat flux. These devices enclose a working fluid within a confined chamber and take advantage of the capillary pressure developed within a porous wick lining to passively transport fluid from the condenser section to the evaporator section. Operating in this fashion, heat can be continuously absorbed and released remotely through near isothermal two-phase transfer at the saturation temperature, drastically reducing the associated temperature drop compared to a solid heat conductor. The porous wick material is commonly composed of sintered copper wire mesh screens or sintered spherical powder, and can have different pore sizes. Understanding the performance limitations imposed on the heat pipe operation by the available capillary pressure and the wick permeability has been the focus of past investigations. Means to decrease the local thermal resistance across the wick thickness in the evaporator and condenser sections under evaporative conditions have also been investigated.

Pruzan et al. [1] developed an analytical prediction of the capillary dryout heat flux for sintered powder wick heat pipes that was corroborated by experiments. This dryout prediction was based solely on the pressure drop in the heat pipe and can be readily and accurately predicted when the capillary pore radius and permeability of the wick material are well defined [2–4]. Wang and Peterson [5] developed a two-dimensional analytical model of a square sintered powder evaporator region and calculated the maximum heat flux capacity based on the pressure drop through the porous layer. It was found that increasing the thickness of the porous layer would correspondingly increase the maximum heat flux based on a capillary limit. However, increases in the layer thickness lead to an increased surface superheat due to the added conduction resistance. Iverson et al. [6] developed a facility which replicated the internal conditions of a heat pipe in order to quantify the contributions to heat and mass transport along the evaporator, condenser, and adiabatic portions of a sintered powder wick. The effective conductivity of the heat pipe system was determined for different wick properties, and the primary mode of heat dissipation from the source was confirmed to be via latent heat removal at the evaporator. Other investigations have focused on the minimization of the evaporation resistance from sintered powder layers. Idealized models of packed sphere beds [7,8] suggested that

* Corresponding author. Tel.: +1 765 494 5621.

E-mail address: sureshg@purdue.edu (S.V. Garimella).

Nomenclature

A_c	cross-sectional area of the copper heat source (heat input area)	x	x -coordinate
D	particle diameter	<i>Greek symbols</i>	
g	acceleration due to gravity	σ_1	liquid surface tension
h_{fg}	latent heat of vaporization	ε	volumetric porosity
K	permeability	ρ_1	liquid density
k	thermal conductivity	μ_1	liquid dynamic viscosity
l_{eff}	liquid working distance	<i>Subscripts</i>	
\dot{m}	evaporation mass flux	Cu	copper
ΔP	pressure drop	c	capillary
q''	heat flux	g	gravitational
R	thermal resistance	l	liquid flow resistance
r_{eff}	effective pore radius	s	solder
T	temperature	sample	test sample
T_{melt}	melting temperature of solder	substrate	copper wick substrate
T_{ref}	vapor reference temperature	x	x -direction
t	material thickness		
U	uncertainty		

optimum particle sizes and porosities exist which maximize the amount of thin-film area from which evaporation occurs. These studies also concluded that minimizing the particle layer thickness can reduce the conduction thermal resistance below the evaporating meniscus.

Recent developments such as multi-core processors and other non-uniform heat flux applications demand adaptive hot-spot cooling solutions. Low-profile vapor chamber heat spreaders, which operate on the same principle as heat pipes, provide an attractive alternative to solid copper heat spreaders, with greatly improved spreading capability. The fluid working distance in such heat-spreading applications is typically much less than in a typical heat pipe used to carry heat to remote condenser locations. Therefore, the limitations to the operation of such vapor chambers are governed more by the boiling heat transfer limit than by the bulk fluid transport (capillary) limit. For applications in which local heat fluxes demand in excess of 500 W cm^{-2} may be encountered, understanding the incipience of boiling, thermal resistance during boiling, local dryout limitations, and the dependence of these quantities on the wick properties, are important areas for investigation.

Chien and Chang [9] studied the thermal resistance of sintered powder wick layers undergoing boiling of water. Sintered wick coatings with average particle diameters of 115 and 247 μm and layer thicknesses of 0.55 and 0.95 mm were tested and it was proposed that an optimum layer thickness-to-particle diameter ratio exists. For the condition where the wick is submerged in the working fluid, optimum performance was obtained for a wick with a thickness-to-particle diameter ratio of 3.85 (0.95 mm/247 μm), an intermediate value in the range investigated. This arrangement subjects the wick to a different fluid feeding mechanism than is encountered in a vapor chamber and the results from this study may thus not be applicable to vapor chambers. Zhao and Chen [10] developed an experimental facility to evaluate the boiling resistances and maximum performance limitations of sintered powder structures. The facility allowed the test fluid, water, to feed into the wick by capillary action to a small heated section above the bulk fluid level. This feeding mechanism mimics the presence of a liquid-vapor free surface in the wick of an operating heat pipe. The study focused on optimization of a grooved non-conventional sintered structure but also evaluated limited evenly dispersed sintered samples. Both the dryout heat flux and thermal resistance performance were found to be superior for a 0.5 mm thick layer

of 50 μm particles compared to a 3 mm thick layer; the thinner layer achieved a maximum heat flux greater than 100 W cm^{-2} . The distance between the water reservoir and the heated section, however, had a strong correlation with the performance, suggesting that capillary feeding limitations may have governed the maximum performance. Davis and Garimella [11] developed a novel thermosyphon facility to determine the thermal resistance of a monoporous sintered powder wick which was fed across a short capillary working distance. Several sintered copper powder samples of varying properties were tested but differences in behavior of the samples was within experimental uncertainty.

Semenic and Catton [12] performed a series of studies on biporous sintered wicks consisting of agglomerated clusters of small particles. The wick thickness, powder size, and cluster size were varied to evaluate the effects on the thermal resistance and boiling limitations. It was observed that for a constant powder size, an increase in the wick thickness extended the maximum dryout heat flux by altering the boiling mechanism within the wick. The biporous sintered wick sample with the best performance dissipated 523 W cm^{-2} at 49 °C of surface superheat. Optimum geometrical parameters for achieving the lowest thermal resistance were not identified. Li et al. [13–15] undertook a set of studies to determine the effects of varying wick thickness, porosity, and pore size on thermal resistance and critical heat flux for screen meshes. In addition to understanding these parametric effects, visual observation of the wicks provided insight into the regimes of evaporation and boiling from these structures at different positions in the acquired boiling curves.

Although monoporous sintered powder wicks are among the more commonly used materials in commercial high-performance heat pipes, the effects of the different wick parameters such as pore size, particle diameter and layer thickness for such wicks under conditions of capillary-fed operation are not yet rigorously understood. In the present work, a test facility is developed that can evaluate the performance of a wick material under conditions of fluid feeding through capillary action and a saturated vapor ambient that simulate an operating vapor chamber or heat pipe. The wick resistance can thus be evaluated in a manner that is independent of capillary limitations on fluid transport in the wick. Fig. 1 shows a cross-section of a vapor chamber with the important thermal resistances in the system highlighted. The test facility is specifically designed to measure the total thermal resistance ($R_{COND,WALL} + R_{COND,WICK} + R_{EVAP/BOILING}$) at the evaporator of the

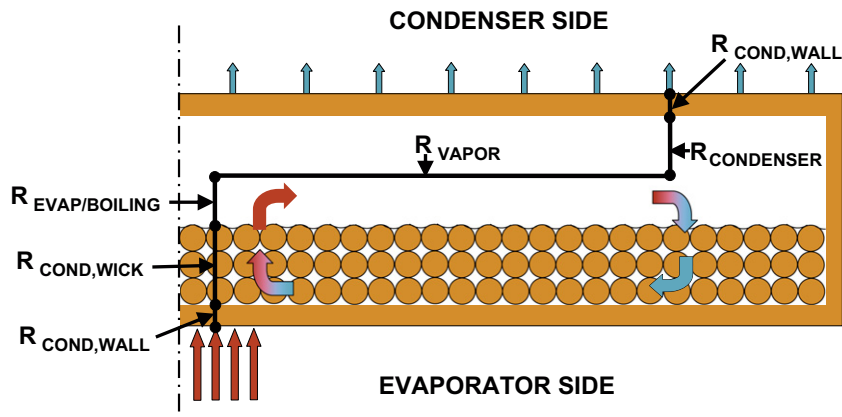


Fig. 1. Cross-section of a vapor chamber showing the important thermal resistances.

device over a range of heat fluxes. The facility is also designed to allow for visualization of the evaporation/boiling process in the wick structure simultaneously with the thermal resistance measurements.

2. Experimental facility, sample preparation, and test procedures

The rationale for the design of the test facility was to simulate the internal conditions of an operating heat pipe evaporator section and supply the working fluid (deionized water) to the porous wick surface in the same manner as occurring within an actual heat pipe. The sub-sections below describe the test chamber and liquid flow loop design which reproduces such conditions.

2.1. Test chamber, heater block assembly, and flow loop details

Detailed diagrams of the test chamber and heater block assembly are shown in Fig. 2(a). The test chamber provides a saturated environment into which the sample dissipates heat and also allows for capillary-fed operation of the wick. The outer chamber walls are constructed from 19 mm (0.75") thick PEEK (polycarbonate is used for two of the walls) to provide insulating walls, while at the same time allowing for visualization of the internal liquid level. The walls are assembled and tightly sealed with silicone o-rings and Teflon gaskets. A pressure transducer monitors the internal chamber pressure which is maintained at atmospheric pressure by leaving the valve to the Graham condenser open to atmosphere during operation of the facility. The Graham condenser serves to re-condense the water vapor back into the chamber while simultaneously allowing non-condensable gases to be purged during degassing. Water flows into the bottom of the chamber after being preheated to the saturation temperature of 100 °C. In this manner, a saturated vapor environment is maintained in the test chamber for the evaluation of all wick samples. Moreover, the test chamber consistently operates at a single saturation pressure and temperature and allows for an easier evaluation of different wick samples over a range of heat inputs, unlike a heat pipe in which the saturation conditions would vary based on the heat input.

To reproduce the wick feeding and evaporation/boiling mechanisms occurring in a heat pipe, the liquid level in the test chamber is maintained at a fixed height throughout the duration of each test by means of a carefully located drain on the side wall. The liquid level is chosen so that the lower edge of the vertically oriented wick surface is submerged in the liquid while the 5 mm × 5 mm heat input area is raised above the liquid surface. The distance from the liquid free surface in the chamber to the center of the 5 mm × 5 mm heat

input area is 8.25 mm. This distance is kept to a minimum so that the performance is not restricted by potential capillary limits. The thermal resistance and the maximum sustainable heat flux measured with the current facility are therefore directly indicative of the evaporation or boiling characteristics of the wick sample. A thermocouple mounted to a translating micrometer stage is placed directly in front of the evaporating sample surface. It is fed through the chamber wall with a dynamic o-ring seal. This allows for the thermocouple to be positioned at a constant separation distance from the sample surface for different porous sample thicknesses; the arrangement also allows for the temperature distribution in the test chamber to be mapped at increasing distances from the sample surface. For all tests in this study, the reference chamber temperature is considered to be the value measured 1 mm from the sample surface; in all cases, this reference temperature was found to be almost identical to the saturation temperature.

The heater block insulation assembly and its interface with the chamber wall are illustrated in Fig. 2(b). Since the outer periphery of the sample is pressed with a silicone o-ring against the chamber wall to form a seal around the wick surface, a 2.54 mm smooth border is maintained around the wick sample onto which no copper powder is sintered. The heat input is generated by four 100 W, 1/8" Watlow FIREROD® cartridge heaters embedded into the back end of a copper block of cross-section 15.875 by 15.875 mm. This cross-section is then reduced to 5 by 5 mm over a 32 mm length through which the heat flux is concentrated and conducted to the back of the sample. Four T-type thermocouples are inserted into 1.19 mm diameter holes manufactured into the tip at a uniform separation distance of 7.62 mm. The last thermocouple, T_4 is 2.54 mm from the tip. The heat flow in this tip is observed from the thermocouple measurements to be one-dimensional for all the tests; the measured, linear temperature gradient can thus be used to calculate the supplied heat flux as well as to estimate the substrate temperature by extrapolation. The entire copper heater block is insulated with at least 25.4 mm of Cotronics Rescor™ 914 ceramic ($k = 0.4 \text{ W m}^{-1} \text{ K}^{-1}$) on all sides. The ceramic insulation is further encased in a 6.35 mm thick layer of PEEK.

The outer flow loop which supplies the test chamber with saturated liquid during testing is shown in Fig. 2(c). A Micropump® (Model GB-P23) gear pump is used to circulate fluid through the flow loop and the flow rate is measured with a 10–100 ml/min McMillan microturbine flowmeter (S-114). The fluid loop passes through a 15 µm Swagelok particulate filter; a 1200 W inline heater is used to preheat the fluid to close to its saturation temperature before it enters the test chamber. Upon exiting the test chamber, the fluid is cooled with a stainless steel liquid-to-air heat exchanger and then returns to the pump.

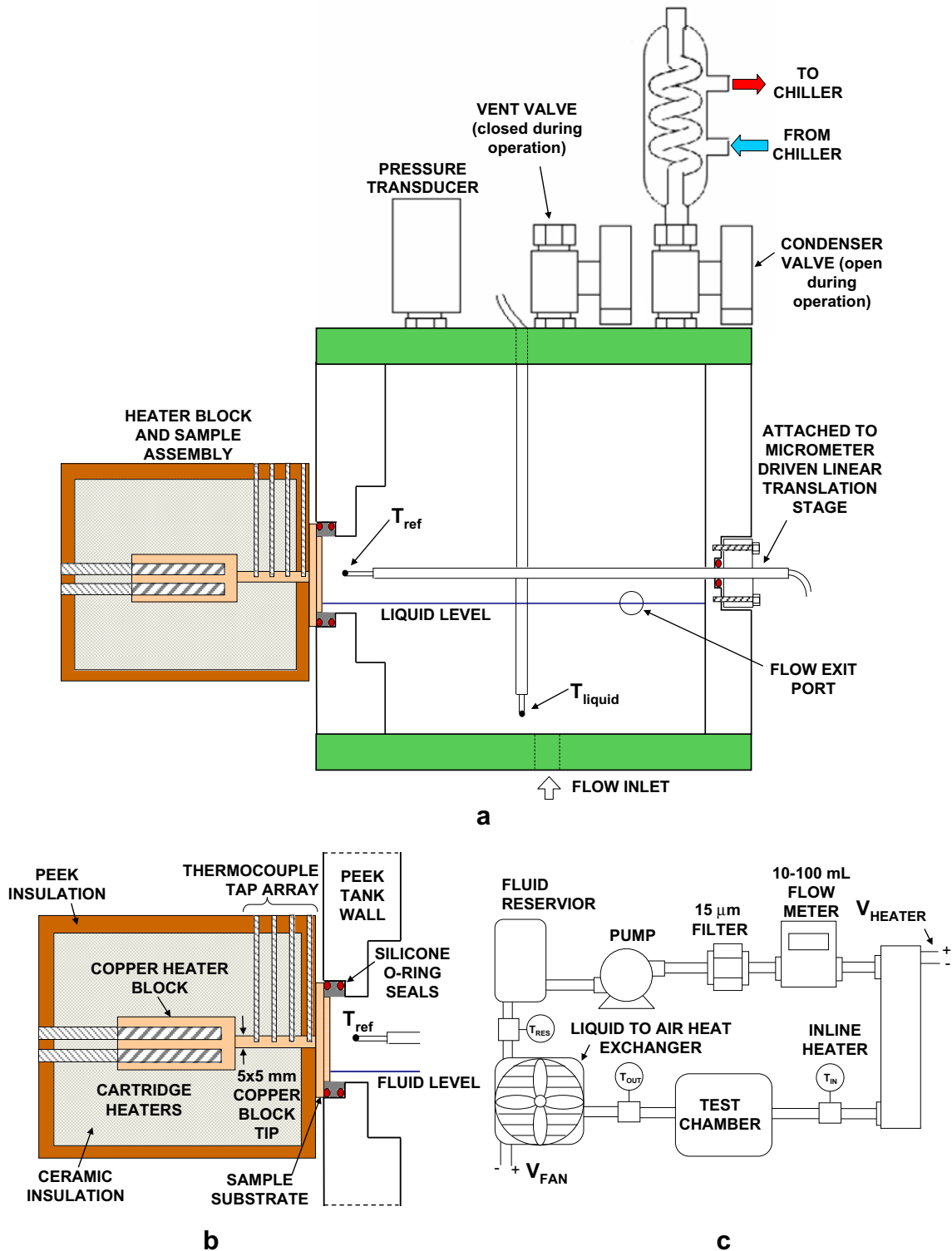


Fig. 2. Diagrams of (a) the test chamber, (b) the heater block and sample assembly, and (c) the test facility flow loop.

2.2. Sample fabrication

All of the sintered copper powder wicks investigated in this study were manufactured at Thermacore, Inc. A layer of copper powder of the desired uniform thickness was sintered on to a square solid copper substrate using a high-temperature mold. The dimensions of the substrate and sintered copper powder layer

are shown in Fig. 3(a). The smooth outer edge of the sample used for sealing against the test chamber is depicted here. A set of nine samples was fabricated with three different layer thicknesses and three different particle sizes, as summarized in Table 1. The range of particle sizes chosen is representative of sintered wicks used in commercial applications. For all of the wick samples, the porosity was maintained constant by sintering particles at their natural

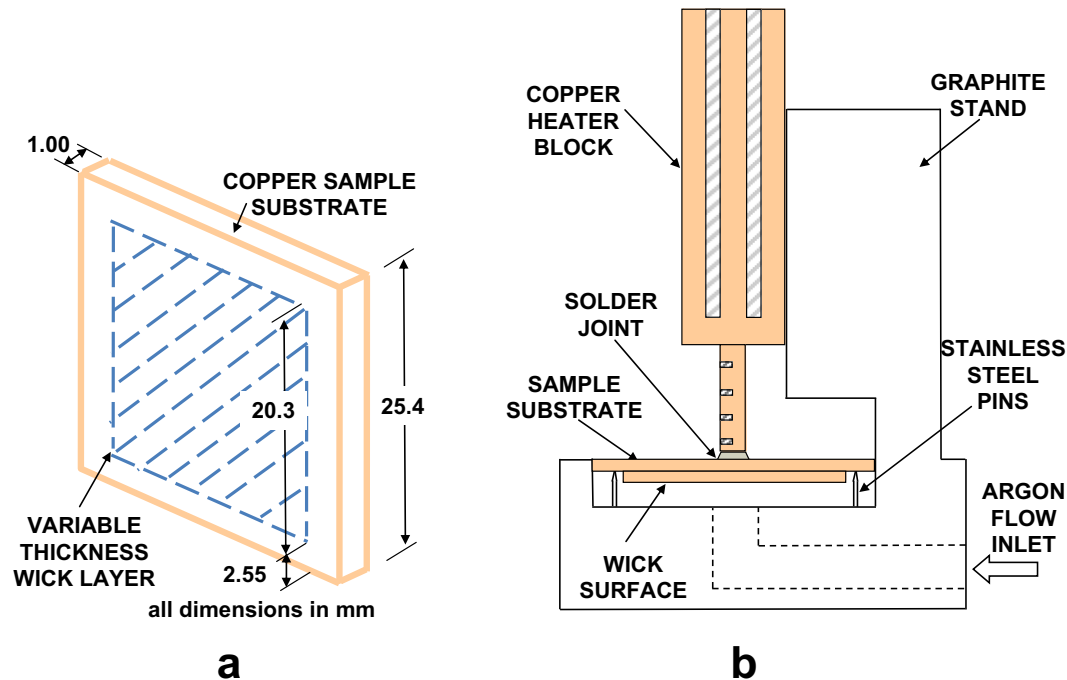


Fig. 3. Diagrams of (a) the sintered copper wick test sample where the dashed region indicates the location of the sintered wick sample and (b) the graphite soldering stand used for proper alignment of the solder joint. The 0.102 mm thick layer of solder is made of Pb–Sn–Ag–Sb (62–35.75–2–0.25%) and has a low melting temperature ($T_{\text{melt}} = 178\text{ }^{\circ}\text{C}$) and a thermal conductivity of $50\text{ W m}^{-1}\text{ K}^{-1}$.

Table 1
List of the sintered copper powder samples tested and their geometric properties.

Sample	US sieve size	Particle diameter range (μm)	Thickness (μm)	Porosity, ϵ^a
45–75:600			600	0.647
45–75:900	(–200 + 325)	45–75	900	0.647
45–75:1200			1200	0.654
106–150:600			600	0.647
106–150:900	(–100 + 140)	106–150	900	0.641
106–150:1200			1200	0.635
250–355:600			600	0.652
250–355:900	(–45 + 60)	250–355	900	0.644
250–355:1200			1200	0.635
250–355:600b	(–45 + 60)	250–355	600	0.657

^a Porosity obtained from post sintering weight per volume measurement.

packing density of approximately 0.35, so that the porosities were approximately 0.65. An additional sample of wick 250–355:600 was used for detailed high-speed camera visualization and identification of the regime of phase change (evaporation or boiling).

Each sample is attached to the heater block made from oxygen-free copper with a tip area of $5\text{ mm} \times 5\text{ mm}$. A solder joint is used for this attachment so as to ensure a significantly higher thermal conductivity interface, and also one with a more uniform and known thickness, compared to thermal greases, pads, and other common interface materials. The higher conductivity and the well-defined and minimized thickness of this interface are critical for minimizing the uncertainty in estimating the temperature drop across this interface, especially at the high heat fluxes investigated in this study. The graphite stand used to achieve a solder joint of uniform thickness is shown in Fig. 3(b). The sample is placed face-down into a recessed pocket in the graphite mold and is held off the surface of the mold by stainless steel pins which hold up the four corners of the exposed substrate. A 0.102 mm thickness square of ribbon solder ($k_s = 50\text{ W m}^{-1}\text{ K}^{-1}$) is placed in the center of the wick sample and is weighted down by the copper heater block. The graphite stand holds the heater block rigidly and

ensures that the joint is formed exactly at the center of the sample as is required for proper alignment when sealing the sample into the test facility. Before heating the solder joint, the sample surface is purged with argon supplied from a compressed gas line that is fed directly into the recessed pocket. This prevents severe oxidation of the porous copper surface that would otherwise occur if it is left in contact with air. In the presence of gas purging, the cartridge heaters in the copper heater block are used to bring the copper assembly to a temperature that is $20\text{ }^{\circ}\text{C}$ above the solder melting temperature of $178\text{ }^{\circ}\text{C}$, allowing the solder and flux to freely flow in the joint and fill all voids. The inert argon atmosphere is maintained until the sample cools down to room temperature. Following the soldering process the sintered copper powder layer retains its original natural salmon color, indicating that oxidation of the surface has indeed been limited. Post-test destructive inspection of this solder joint reveals no significant void areas.

2.3. Test procedures

Immediately prior to insertion into the test facility, all soldered samples are treated to remove any possible grease contamination

or minor surface oxidation that may have occurred. These kinds of surface contaminants are known to strongly affect the surface wetting of copper wick materials [16]. For this treatment, the samples are dipped in acetone and thoroughly rinsed with deionized (DI) water to remove any embedded grease. The samples are subsequently dipped in a dilute acid piranha etch solution and rinsed with DI water to strip the surface of further contaminants and oxide layers, returning any minor discolorations on the sample surface to their native salmon-colored appearance. This method has been previously used for pre-test treatment of sintered copper powder wick materials [17]. All of the sample preparation protocols are strictly followed for each tested sample to ensure reliable and repeatable test results.

At the start of each test, the sample is sealed into the facility and the chamber is filled with fresh DI water from the reservoir. To degas the liquid, the flow rate and inline heater power are set such that the inline pre-heater (Fig. 2(c)) causes vigorous boiling; the condenser allows the non-condensable gases to be purged from the test chamber during this process. Once degassing is completed, the inline heater voltage is reduced such that liquid water is flowing into the tank at the saturation temperature. This liquid heating and flow rate are carefully controlled such that large vapor bubbles do not flow out of the pre-heater and into the chamber, which would cause perturbations in the liquid free surface and thus affect the precise setting of the liquid level along the sample surface in the test chamber.

Each individual heat flux setting is achieved by first supplying an overshoot wattage to the cartridge heaters to rapidly raise the heat flux to the desired level. This wattage is then reduced and adjusted to the value that results in the desired heat flux being set under a steady state. This overshoot method brings the system and heater block, with their large thermal mass, to a steady state more rapidly, drastically reducing the overall test duration. A steady state is defined to have been reached when the substrate temperature changes at a rate of less than 0.05 °C/min time-averaged over a period of 10 min. In most cases, this temperature change stabilizes at under 0.01–0.03 °C/min. The supplied heat flux is increased in increments to acquire different test data points for developing a boiling curve.

3. Data reduction and measurement uncertainties

The recorded temperatures are averaged over the final 100 data points (5 min) of the acquired steady-state data. Details of the temperature measurement locations are shown in Fig. 4; also denoted in the figure is the terminology for the extrapolated temperatures. Assuming one-dimensional conduction in the heater tip, the heat flux supplied to the sample can be calculated from:

$$q''_x = -k_{Cu} \frac{dT}{dx}, \quad (1)$$

in which the gradient is calculated as the slope of a linear fit to the measured temperatures at known x -locations. This heat flux repre-

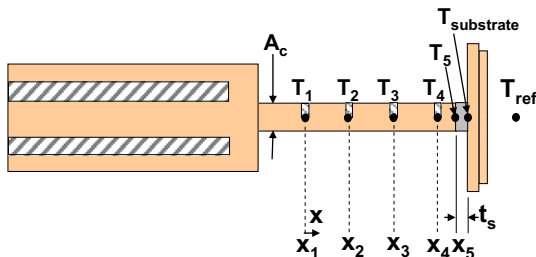


Fig. 4. Diagram of the copper heater block temperature measurement locations and nomenclature.

sents only the heat being transported directly through the copper extension and out through its tip, and accounts for all the heat losses through the heater block insulation with respect to the electrical power input. The temperature at the back of the copper substrate can then be calculated by extrapolation using

$$T_{\text{substrate}} = T_4 - q''_x \left[\frac{(x_5 - x_4)}{k_{Cu}} + \frac{t_s}{k_s} \right], \quad (2)$$

because the cross-sectional area remains uniform up to this location. Spreading by lateral conduction in the copper substrate prevents further one-dimensional extrapolation of the temperature field to the front surface of the substrate. Moreover, the heat transfer coefficient distribution on the wick surface is unknown, which precludes a computation of the temperature profile and spreading resistance within the substrate. Therefore, the results presented include this additional conduction resistance through the copper substrate; the calculated sample resistance is defined as

$$R_{\text{sample}} = \frac{T_{\text{substrate}} - T_{\text{ref}}}{q''_x A_c}. \quad (3)$$

This performance metric effectively treats the sample substrate as if it were a vapor chamber wall with a small heat source representing the evaporator heat input; lateral spreading by conduction in the substrate is included in this metric.

A comprehensive uncertainty analysis is performed and all the reported results include these uncertainty estimates. The uncertainty in the calculated heat flux is estimated by evaluating the uncertainty intervals for the slope and intercept of the linear fit to the temperature field in the heater block [18]. This uncertainty in heat flux is then used to calculate uncertainties in the substrate temperature and the sample resistance using a standard approach as follows:

$$U_R^2 = U_{T_{\text{substrate}}}^2 \left(\frac{1}{q''_x A_c} \right)^2 + U_T^2 \left(\frac{1}{q''_x A_c} \right)^2 + U_{q''_x}{}^2 \left(\frac{T_{\text{substrate}} - T_{\text{ref}}}{q''_x A_c} \right)^2, \quad (4)$$

$$U_{T_{\text{substrate}}}^2 = U_T^2 + U_{q''_x}^2 \left(\frac{(x_5 - x_4)}{k_{Cu}} + \frac{t_s}{k_s} \right)^2 + U_x^2 \left(\frac{q''_x}{k_{Cu}} \right)^2 + U_{t_s}^2 \left(\frac{q''_x}{k_s} \right)^2. \quad (5)$$

All thermocouples utilize an external ice point reference junction resulting in an estimated temperature measurement uncertainty, U_T , of ± 0.3 K. The x -location measurement uncertainty, U_x , is ± 0.20 mm and is attributed to the tolerance in the thermocouple insertion hole dimensions and the bead width. The solder joint thickness uncertainty is estimated to be ± 0.0254 mm, which is 25% of the nominal solder ribbon thickness.

4. Experimental results and discussion

Test results for all the sintered powder wick samples are presented in the form of boiling curves and the variation of thermal resistance with input heat flux; a representative set of such plots for the 900 μm thick samples is shown in Fig. 5. Each data point on these curves represents a steady-state measurement at the given heat flux. The average (and maximum) uncertainties for the heat flux, superheat temperature, and thermal resistance are $\pm 2.1\%$, $\pm 25.5\%$, and $\pm 25.8\%$ ($\pm 3.9\%$, $\pm 38.3\%$, and $\pm 38.2\%$), respectively. The primary contributor to these uncertainty values is the uncertainty in the location of the thermocouples within the tapped holes. None of the figures presented here indicate that a dryout or critical heat flux condition has been reached at the maximum heat flux shown. For all of the samples, the maximum heat flux was instead governed by insulation material temperature limitations within the heater block before a dryout condition and associated temperature excursion was ever observed. All samples are identified in the legends by the particle diameter range and wick thickness (see Table 1 for a summary of sample properties).

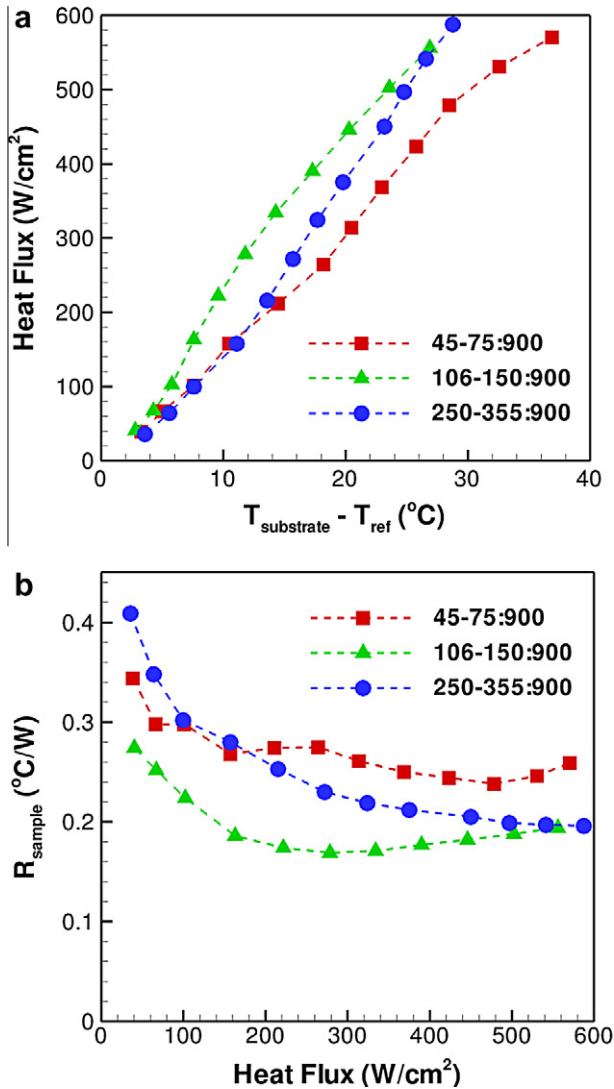


Fig. 5. Steady-state thermal performance results for the 900 μm thickness test samples. The maximum heat flux test point does not correspond to a dryout condition for any of the curves. The results are presented in the form of (a) boiling curves, and (b) calculated sample thermal resistances as a function of heat flux. (Maximum uncertainties: $q'' \pm 11.2 \text{ W m}^{-2}$, $R_{\text{sample}} \pm 0.047 \text{ }^\circ\text{C/W}$, $\Delta T \pm 6.8 \text{ }^\circ\text{C}$.)

Figs. 5(a) and 6(a) show the boiling curve for the set of three 900 μm thickness samples and three 250–355 μm particle sizes, respectively. All samples in this study were able to dissipate a heat flux in excess of 500 W cm^{-2} , with the highest heat flux observed being $596.5 \pm 11.3 \text{ W cm}^{-2}$ for sample 250-355:1200. This is a considerably larger heat flux than has been observed in past studies of monoporous sintered powders and the difference may be attributed, in part, to the short fluid working distance which eliminates any capillary feeding limitations. A conservative estimate for the capillary limit of the test facility configuration can be obtained by supposing that all the evaporated liquid mass flux for a given heat flux,

$$\dot{m} = \frac{q'' A_c}{h_{fg}}, \quad (6)$$

must travel linearly up the sample surface to the top of the heat input region. The available capillary pressure,

$$\Delta P_c = \frac{2\sigma_1}{r_{\text{eff}}}, \quad (7)$$

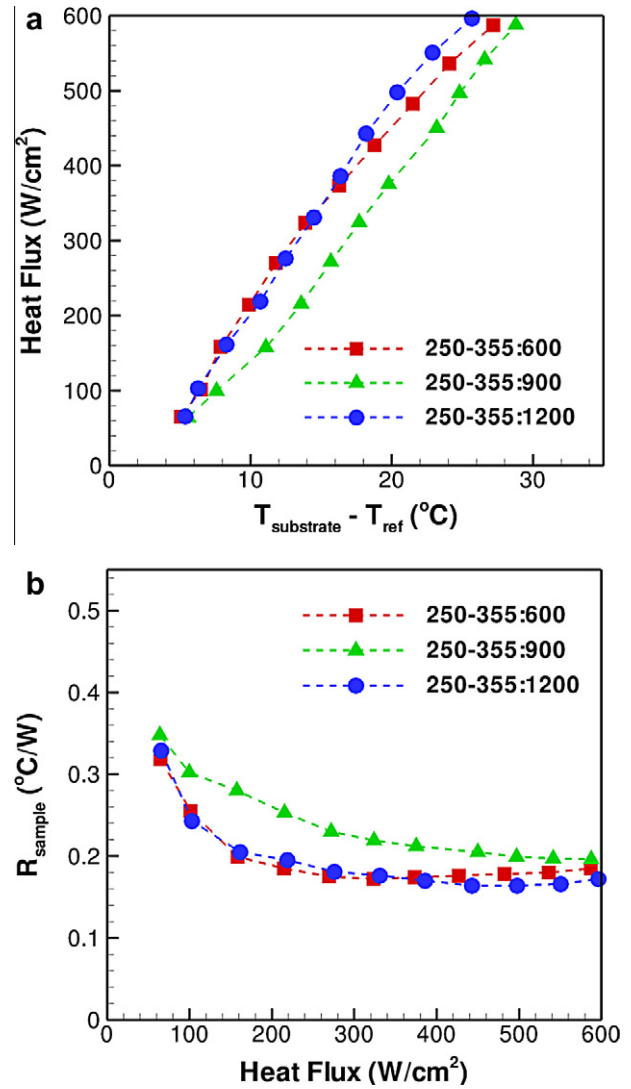


Fig. 6. Steady-state thermal performance results for the 250–355 μm diameter particle test samples. The results are presented in the form of (a) boiling curves, and (b) calculated sample thermal resistances as a function of heat flux. (Maximum uncertainties: $q'' \pm 11.3 \text{ W m}^{-2}$, $R_{\text{sample}} \pm 0.047 \text{ }^\circ\text{C/W}$, $\Delta T \pm 6.9 \text{ }^\circ\text{C}$.)

can be compared to the sum of the pressure drops due to frictional resistance to liquid flow and gravitation,

$$\Delta P_1 + \Delta P_g = \frac{\mu_l l_{\text{eff}} \dot{m}}{\rho_l K A} + \rho_l g l_{\text{eff}}, \quad (8)$$

for the given wick properties [19],

$$r_{\text{eff}} = 0.21D, \quad (9)$$

$$K = \frac{D^2 \varepsilon^3}{150(1 - \varepsilon)^2}. \quad (10)$$

For the most limiting powder geometry case at 500 W cm^{-2} (sample 45-75:600), the available capillary pressure (11,430 Pa) remains an order of magnitude larger than the opposing single-phase pressure drop calculated from Eq. (8) (1070 Pa). Any observed dryout in the tests conducted in the present study would thus be solely due to a boiling limit. It may thus be concluded that the boiling limit for all sintered powders investigated in this work exceeds the maximum tested heat fluxes. The difficulty in experimentally producing higher heat flux inputs prevents a precise evaluation of the effect of the powder particle diameter and wick thickness on dryout. It is,

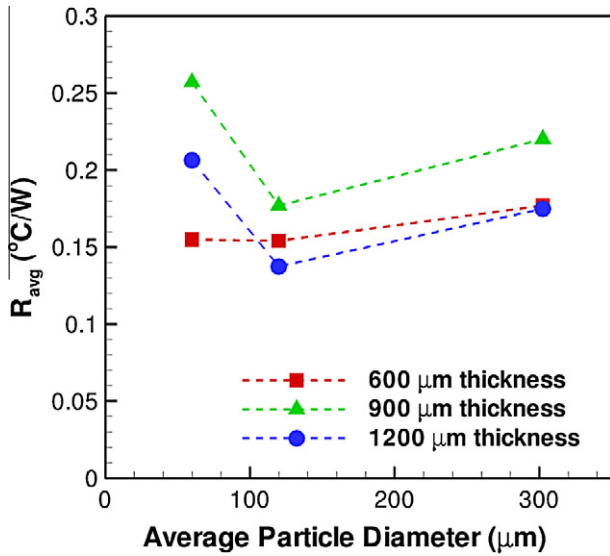


Fig. 7. Average boiling thermal resistance for all 9 test samples as a function of the average sample particle size. (Maximum uncertainties: $q'' \pm 11.6 \text{ W m}^{-2}$, $R_{\text{sample}} \pm 0.047 \text{ }^\circ\text{C/W}$, $\Delta T \pm 7.1 \text{ }^\circ\text{C}$.)

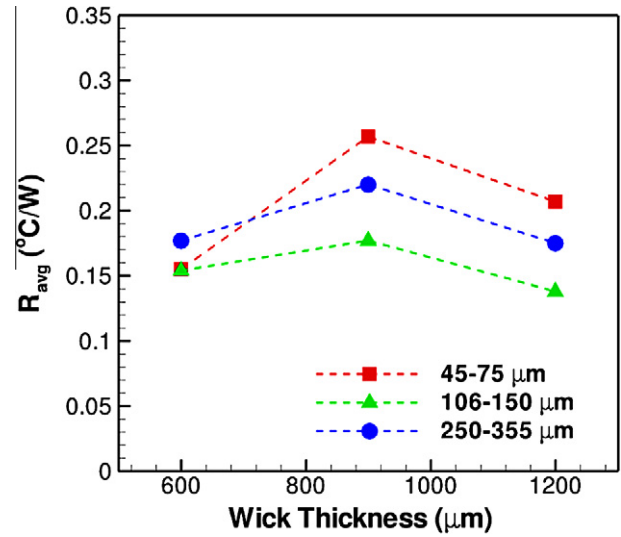


Fig. 8. Average boiling thermal resistance for all 9 test samples as a function of the sample wick thickness. (Maximum uncertainties: $q'' \pm 11.6 \text{ W m}^{-2}$, $R_{\text{sample}} \pm 0.047 \text{ }^\circ\text{C/W}$, $\Delta T \pm 7.1 \text{ }^\circ\text{C}$.)

nonetheless, noteworthy that when tested without the occurrence of capillary limitations, standard sintered powder wicks can support local hot-spot heat flux densities in excess of 500 W cm^{-2} without the initiation of dryout.

The calculated thermal resistances of these different test samples are presented in Figs. 5(b) and 6(b) as a function of heat flux. A lower resistance corresponds to a more favorable overall heat transfer coefficient from the substrate to the ambient vapor. The trends observed in these figures are consistent across all the samples tested. At the lower heat inputs, the resistance is higher, and decreases as the heat input is increased. Qualitative observation of the surfaces shows that the low-flux test points, categorized as those less than $\approx 75 \text{ W cm}^{-2}$, correspond to evaporative conditions prior to the observation of bubble nucleation from the sample surface. Once bubble nucleation commences and boiling is established with an increase in the heat flux, the overall resistance reduces to a minimum value and remains relatively constant as the region of the sample surface undergoing boiling increases. The minimum

measured resistance of any of the tested samples was observed to be $0.130 \pm 0.047 \text{ }^\circ\text{C W}^{-1}$ at a heat flux of $333.6 \pm 6.4 \text{ W cm}^{-2}$ for sample 106-150:1200. Considering that a part of this resistance is due to conduction resistance offered by the substrate (less than $0.100 \text{ }^\circ\text{C W}^{-1}$ that would result from a limiting assumption of 1D conduction through the substrate), the resistance due to boiling in the wick is significantly lower than these measured (substrate and wick) resistance values.

In almost all cases, a slight increase in the resistance is observed at the highest heat fluxes tested. The increase is likely induced as the sample experiences dryout conditions over some regions, leading to localized vapor blanketing and a concomitant increase in the average surface temperature. This mechanism is supported by the observation of an increase in small temperature spikes in the transient substrate temperature data at these higher fluxes. However, a non-recoverable temperature overshoot was never observed. A more detailed investigation into the relationship between the thermal resistance and the observed evaporation/boiling regimes is presented in Section 4.3.

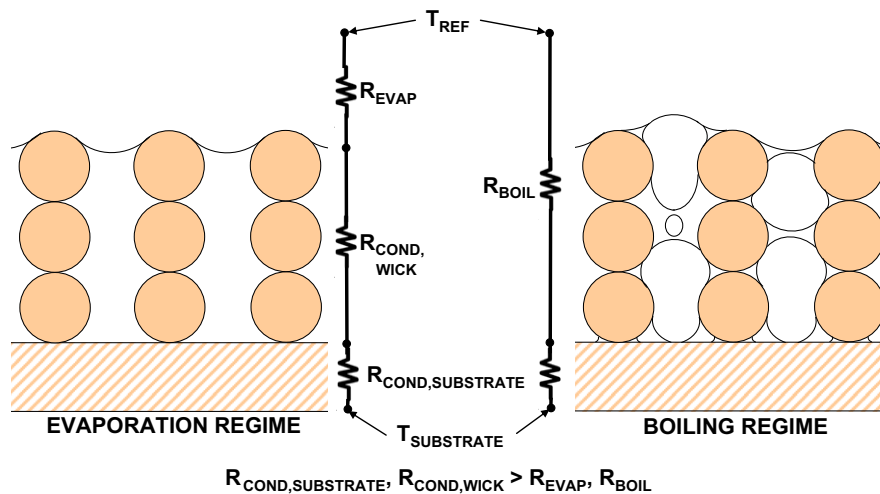


Fig. 9. Schematic illustration of the visualized two-phase regimes for wicked evaporation and boiling. Resistances to heat flow are also conceptually indicated to explain the heat transfer mechanisms.

4.1. Effect of particle size on thermal performance

The thermal performance of all three 900 μm thickness samples is compared in Fig. 5(b) to distinguish the impact of varying particle size. Similar trends as seen in this figure were also found for the 600 μm and 1200 μm thick samples. A minimum resistance is exhibited by the intermediate particle size, suggesting that an optimal pore size may exist for maximizing the boiling heat transfer coefficient. This relationship is more clearly shown when the thermal resistance is plotted as a function of particle size for all the samples tested, as shown in Fig. 7. Each point on this plot corresponds to the averaged resistance over the nucleate boiling regime (200–500 W cm^{-2}) for each sample. The average particle diameter is taken as the mean of the minimum and maximum particle sizes contained in each sample. The values at heat fluxes at which the wicks experience only evaporative heat transfer, as well as those at the other end of the heat flux range, where partial dryout may have occurred, are omitted from this averaging, since the focus in this comparison is on the performance in the boiling regime. However, the trends are unchanged if averaged values over the entire heat flux range are included. The same is true if only the minimum measured resistance for each sample were plotted.

The sample resistance is seen to decrease when the particle size is decreased from 355 to 106 μm (effective pore diameters from 150 to 45 μm). This result is consistent with Li and Peterson's [14] findings for screen mesh wicks for pore sizes larger than 100 μm . As the pore size is decreased, more surface area is available for heat transfer and an increased number of smaller cavities may support bubble nucleation, both of which would enhance the boiling performance. For the smallest particles considered in the current study (45–75 μm particles with effective pore diameters from 20 to 30 μm), the trend is reversed. A possible explanation for this increase in resistance may be a decreased permeability at these particle sizes. From Eq. (10) for the permeability of a porous sintered material, it is apparent that for particle sizes below 100 μm , a decrease in particle size leads to a rapid reduction in permeability. While this reduced permeability does not precipitate a capillary-limited behavior for single-phase flow, the increased drag resistance on bubble flow and escape from the sample surface may increase the thermal resistance for the smallest particle sizes tested. This explanation is consistent with this effect being the least apparent for the thinnest (600 μm thick) sample, which would pose the shortest path for bubble release. Observations of an optimum wick thickness-to-particle size ratio were made by Chien and Chang [9] for submerged pool boiling from sintered powder wicks, similarly indicating an optimum particle size for a given wick thickness.

4.2. Effect of wick thickness on thermal performance

The effect of wick thickness on the thermal performance is illustrated by comparing the thermal resistances (averaged over the heat flux range of 200–500 W cm^{-2}) for all three particle diameters in Fig. 8. For all particle sizes, the thermal resistance is at a maximum for the median thickness sample and decreases slightly for the 600 and 1200 μm samples. It is noted, however, that the average spread in the results over the set of different samples is approximately 21%, which is less than the experimental uncertainty of 25.8% over this heat flux range. Similarly, the thermal resistance curves (shown in Fig. 6(b) for the largest particle size) also show that the variation of thermal resistance versus thickness is within this experimental uncertainty over the range of heat flux data points greater than 100 W cm^{-2} . For only the 45–75 μm particle diameter samples, the spread in thermal resistance with respect to wick thickness is outside the predicted uncertainty, suggesting a possible dependence of the performance on thickness

for this particle size. The impact of wick layer thickness on the performance is therefore modest in the thickness range of 600–1200 μm investigated here. Li et al. [13] also reported on the relative independence of thermal performance on wick thickness from their tests on sintered screen mesh wicks of varying thickness under similar fluid feeding conditions. Visual observation of the sample surfaces during testing (as discussed in the next section) also confirmed the presence of boiling and bubble departure from the surface of all samples at heat fluxes above 100 W cm^{-2} , independent of thickness.

4.3. Visualization of operating regimes

It was observed from the thermal measurements in the preceding sections that the overall sample thermal resistance is highest at low heat fluxes (when evaporation is the main mode of two-phase transport) and sharply decreases and to a relatively constant value

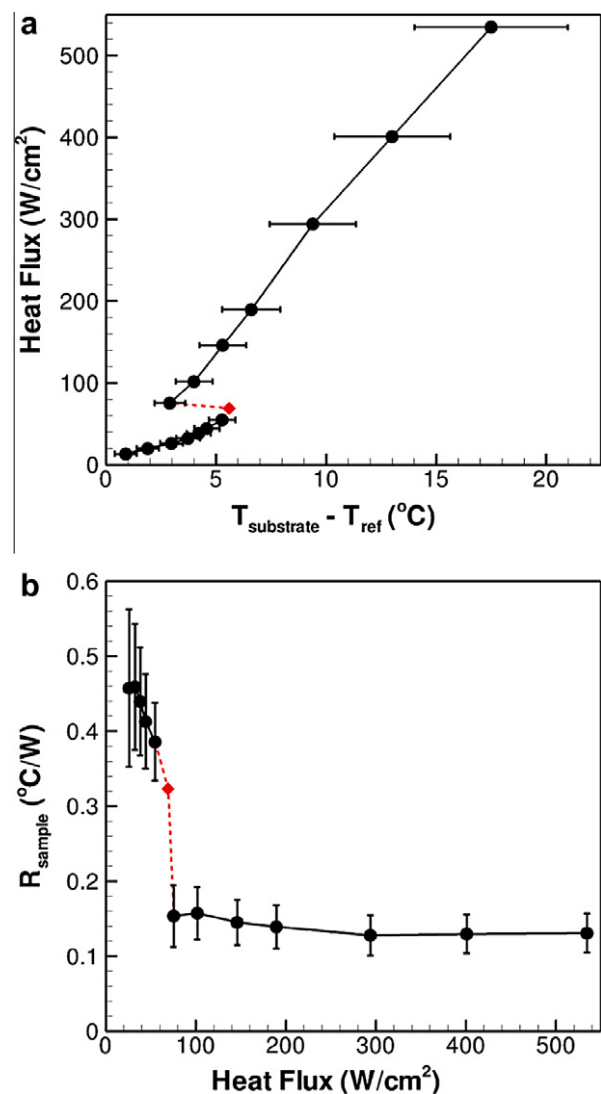


Fig. 10. The boiling curve and the variation of thermal resistance with heat flux for sample 250-355:600b. High-speed visualization of the sample surface during testing confirms that up to a heat flux of 55 W cm^{-2} , only evaporation from the liquid-vapor interface at the top of the wick is present. This is followed by the incipience of boiling at the 75 W cm^{-2} flux. The (red) data point shown as a diamond symbol and the dashed lines represent the heat flux, superheat, and resistance directly prior to incipience of boiling as extracted from the transient test data. (For interpretation of the references to color in this figure legend, the reader is referred to the web version of this paper.)

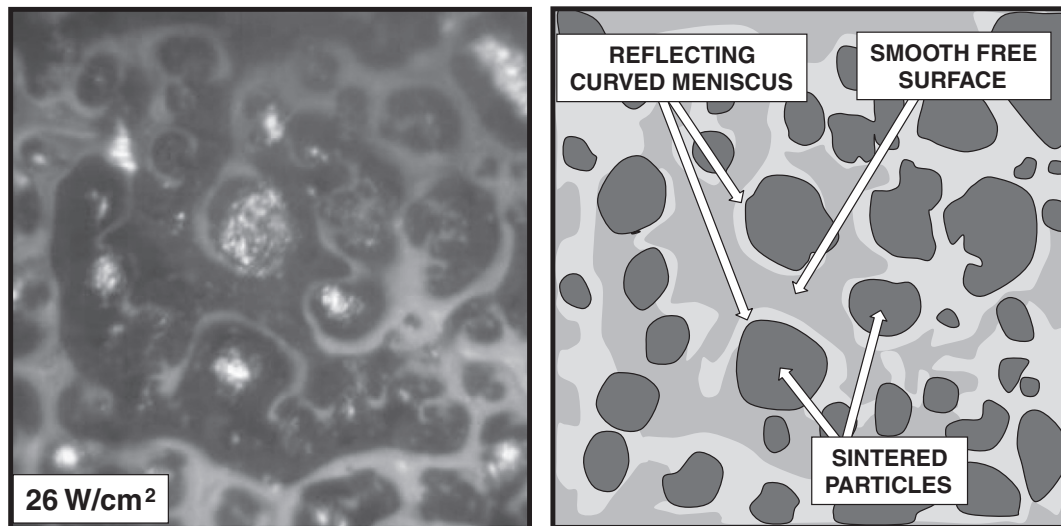


Fig. 11. Image and representative sketch of the fluid free surface and solid particles at a heat flux for which the evaporation regime is sustained for sample 250-355:600b. The top layer of particles can be seen protruding from the liquid free surface with the curved menisci outlined by reflection of the light source. The porous layer is approximately three particle diameters thick.

after the incipience of boiling. During evaporation, there are three main series resistances in the measured overall resistances: conduction and spreading through the substrate, conduction through the saturated wick layer, and thin-film evaporation at the free surface meniscus. A schematic diagram of this two-phase regime and the associated thermal resistances is shown in Fig. 9 (on the left side). As long as the capillary pressure provided by the wick can overcome the pressure losses during evaporation, the fluid level will not recede into the wick (towards the substrate). The thermal resistance due to conduction through the saturated wick layer is expected to be significantly larger than due to thin-film evaporation at the free surface. The dominance of the wick thermal conduction resistance has been highlighted in the modeling of thin-film evaporation from porous media [6,7]. However, during boiling, as supported by the observed independence of thermal resistance on the wick thickness, nucleation occurs at the substrate–wick interface (the hottest part of the wick layer) and eliminates this wick conduction resistance (as shown on the right side of Fig. 9). Therefore, the measured overall thermal resistance during boiling would be reduced by approximately this wick conduction resistance.

A finer resolution of the thermal measurements specifically in the vicinity of the heat flux at which the regime transitions from evaporation to boiling would quantitatively demonstrate this transition. For this reason, an additional test was performed with sample 250-355:600b with a focus in the transitional range of heat fluxes. Also, in order to reduce uncertainty in the measured thermal resistance, the size of the thermocouples and the tapped hole tolerances were reduced, lowering the positional uncertainty in temperature measurement, U_x , to ± 0.08 mm. The test facility was also modified to accommodate a precision borescope attached to a Photron Fastcam Ultima APX high-speed camera. This provided the capability to view the two-phase processes occurring at the sample surface at frame rates of up to 10,000 frames per second. Detailed visualizations of the surface were recorded for each heat flux to aid in verification of the regime-based mechanisms proposed above.

The thermal performance results for this test are presented in Fig. 10. From the boiling curve, a nearly linear rise in the superheat temperature is observed as the heat flux is gradually incremented up to 55 W cm^{-2} . Detailed visualizations of the surface confirm

that heat transfer occurs through evaporation for this range of heat fluxes. For the next heat flux test point, the substrate temperature is maintained for a short time before a sharp decrease in the superheat is suddenly observed corresponding to the nucleation of bubbles from the substrate. The diamond-shaped (red) data point in the figure corresponds to this nucleation, clearly showing the incipience superheat. Following incipience, during the boiling regime, the temperature again steadily rises with heat flux but with an increased slope, indicative of a reduced thermal resistance. This thermal resistance is quantified in Fig. 10(b). In the evaporative regime, the first several data points have a relatively constant resistance between 0.4 and $0.5 \text{ }^\circ\text{C W}^{-1}$. Fig. 11 presents an in situ image of the saturated sample surface after steady state was achieved at a heat flux of 26 W cm^{-2} , characteristic of the regime in which only evaporation occurs. In this image (and the schematic illustration on the right), it is seen that the fluid free surface does not recede into the sintered powder and hence, the conductive resistance through the saturated wick has not significantly changed. Observation of the surface following the sharp decrease in resistance shows bubble departure through a free surface that remains fixed at the top layer of particles.

The series of images in Fig. 12(a) demonstrate the stages of observed nucleation, growth and departure for a single bubble from the wick at the 75 W cm^{-2} test point. These images are taken from a video that is available as [Supplementary data](#) provided with this paper. To improve delineation between the vapor bubble, underlying particles, and fluid surface, a representative sketch of several of the frames is also shown in Fig. 12(b). As the heat flux is increased to the maximum of 535 W cm^{-2} , the bubble departure rate increases but the fluid does not begin to dryout or recede further into the wick. The overall thermal resistance also does not significantly change for the range of heat fluxes for which boiling occurs. These trends illustrate that the relative changes in resistance as the heat flux is varied within the evaporation and boiling regimes are minor compared to the $\sim 0.175 \text{ }^\circ\text{C W}^{-1}$ decrease associated with the transition to boiling. This trend, together with visualization of the wick in these regimes, supports the explanation that this large resistance drop can be attributed to removal of the wick layer conductive resistance once boiling commences. Applying an approximate 1D heat flow analysis over the $5 \times 5 \text{ mm}$ heat input region, this

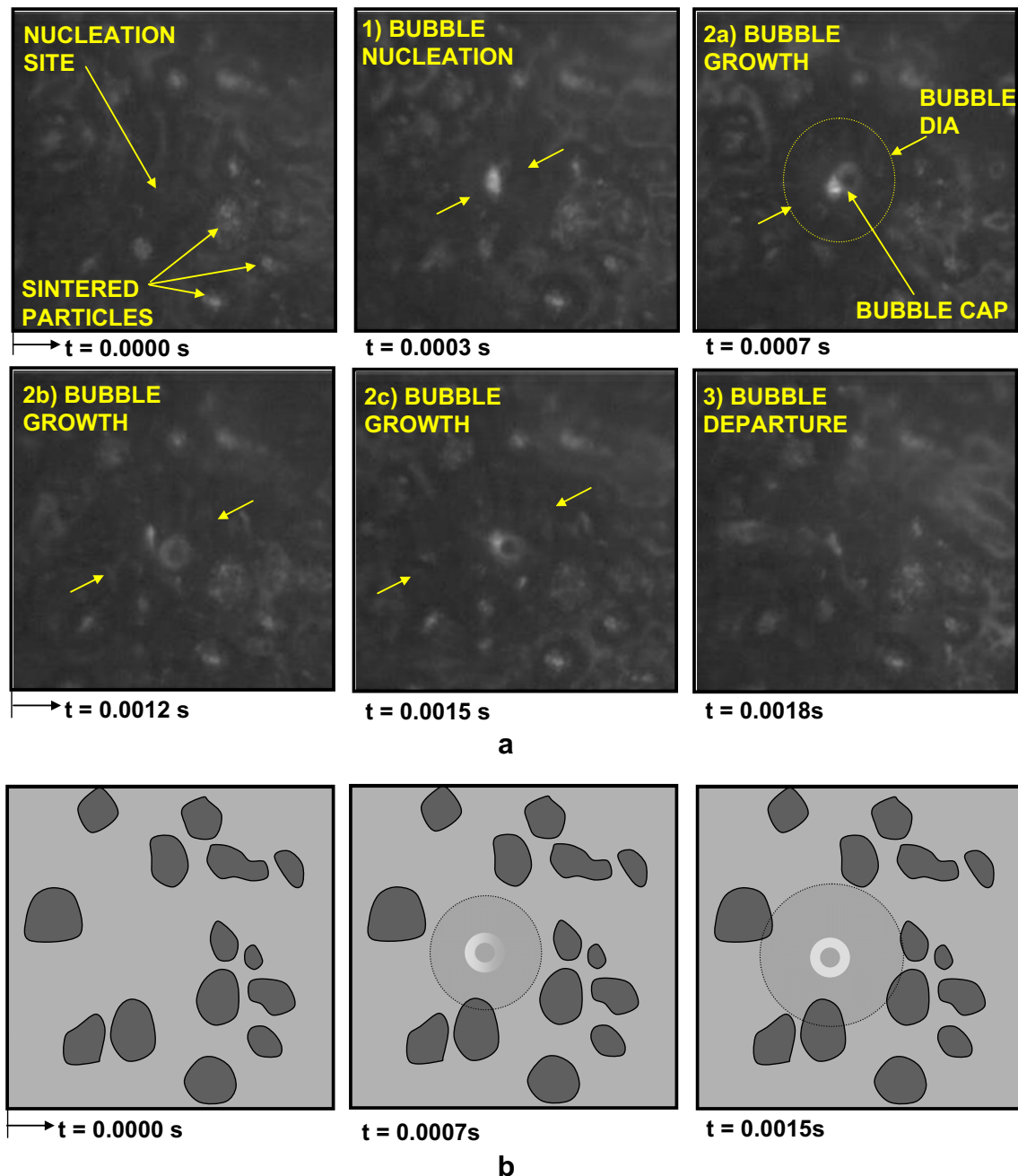


Fig. 12. (a) Series of images documenting growth and departure of a single bubble from a nucleation site within the porous layer for sample 250-355:600b. In the initial frame, the liquid free surface is undisturbed. In the following frames, the arrows point to the bubble diameter as it grows in size before breaking through the free surface and being released. The images are extracted from video recorded at 10,000 frames per second (video is provided as Supplementary data). (b) Representative sketches of the nucleation site (corresponding to upper left image in part (a)) and bubble growth (corresponding to stages 2a and 2c in the photographs).

conductive resistance drop would correspond to an approximate thermal conductivity of $137 \text{ W m}^{-1} \text{ K}^{-1}$ for the $600 \mu\text{m}$ thick porous material. Previous analytical predictions [20] and experiment measurements [4] of thermal conductivity for sintered copper powder wicks of similar porosity as those studied here obtained comparable resistance values, supporting the reason offered for the drop in resistance when transitioning from the evaporation to the boiling regime.

Results from this work thus suggest that a consideration of this fundamental difference between the evaporation and boiling modes of operation of wick structures should be included in the modeling and design of vapor chambers and heat pipes.

5. Conclusions

A novel test facility was developed to characterize the thermal performance of wick structures used in heat pipes and vapor chambers, under operational conditions as seen in the actual devices. A parametric investigation of the dependence of the thermal performance on the wick thickness and the particle size was conducted. In addition, the surface of the wick was observed with high-speed visualization in situ during the testing. The visualized images yielded important insights into the operation of wick structures in heat pipes and vapor chambers. The key conclusions drawn from this work include:

- (1) Typically sized monoporously sintered power wick materials can sustain local heat fluxes of greater than 500 W cm^{-2} without reaching a boiling limit or dryout.
- (2) For a given sintered powder wick thickness, a trade-off between the increased area for heat transfer and increased resistance to vapor flow out of the wick result in the existence of an optimum particle size which minimizes the thermal resistance.
- (3) A sharp reduction in the overall evaporator thermal resistance is observed corresponding to a transition from the evaporation to the boiling regime. This occurs as a result of a transition in the mode of heat transfer from thin-film evaporation at the free surface of a liquid-saturated wick to bubble nucleation at the substrate-wick interface, effectively eliminating the wick conduction resistance.

Acknowledgements

This material is based upon work supported by the Defense Advanced Research Projects Agency (DARPA) and Space and Naval Warfare Systems Center (SPAWAR/SYSCEN) San Diego, CA under Contract No. N66001-08-C-2001.

Appendix A. Supplementary data

Supplementary data associated with this article can be found, in the online version, at doi:10.1016/j.ijheatmasstransfer.2010.05.043.

References

- [1] D.A. Pruzan, L.K. Klingensmith, K.E. Torrance, C.T. Avedisian, Design of high-performance sintered-wick heat pipes, *Int. J. Heat Mass Transfer* 34 (6) (1991) 1417–1427.
- [2] H. Kozai, H. Imura, Y. Ikeda, The permeability of screen wicks, *JSME Int. J., Series 2: Fluids Eng. Thermophys. Prop.* 34 (2) (1991) 212–219.
- [3] H. Kozai, H. Imura, Y. Ikeda, The effective pore radius of screen wicks, *Heat Transfer Eng.* 15 (4) (1994) 24–32.
- [4] Y.-Y. Lin, T. Semenic, I. Catton, Thermophysical properties of monoporously sintered copper, in: *Proceedings of the ASME Summer Heat Transfer Conference*, San Francisco, CA, 2005, pp. 17–23.
- [5] Y.X. Wang, G.P. Peterson, Analytical model for capillary evaporation limitation in thin porous layers, *J. Thermophys. Heat Transfer* 17 (2) (2003) 145–149.
- [6] B.D. Iverson, T.W. Davis, S.V. Garimella, M.T. North, S.S. Kang, Heat and mass transport in heat pipe wick structures, *J. Thermophys. Heat Transfer* 21 (2) (2007) 392–404.
- [7] R. Ranjan, J.Y. Murthy, S.V. Garimella, Analysis of the wicking and thin-film evaporation characteristics of microstructures, *J. Heat Transfer* 131 (2009).
- [8] M.A. Hanlon, H.B. Ma, Evaporation heat transfer in sintered porous media, *J. Heat Transfer* 34 (4) (2003) 644–652.
- [9] L.H. Chien, C.C. Chang, Experimental study of evaporation resistance on porous surfaces in flat heat pipes, in: *Thermomechanical Phenomena in Electrical Systems – Proceedings of the Intersociety Conference*, 2002, pp. 236–234.
- [10] Y. Zhao, C.I. Chen, An investigation of evaporation heat transfer in sintered copper wicks with microgrooves, in: *Proceedings of 2006 ASME International Mechanical Engineering Congress and Exposition*, Chicago, IL, 2006.
- [11] T.W. Davis, S.V. Garimella, Thermal resistance measurement across a wick structure using a novel thermosiphon test chamber, *Exp. Heat Transfer* 21 (2) (2008) 143–154.
- [12] T. Semenic, I. Catton, Experimental study of biporous wicks for high heat flux applications, *Int. J. Heat Mass Transfer* 52 (21–22) (2009) 5113–5121.
- [13] C. Li, G.P. Peterson, Y. Wang, Evaporation/boiling in thin capillary wicks (I) – wick thickness effects, *J. Heat Transfer* 128 (12) (2006) 1312–1319.
- [14] C. Li, G.P. Peterson, Evaporation/boiling in thin capillary wicks (II) – effects of volumetric porosity and mesh size, *J. Heat Transfer* 128 (12) (2006) 1320–1328.
- [15] C. Li, G.P. Peterson, J. Li, N. Koratkar, The visualization of thin-film evaporation on thin micro sintered copper mesh screen, in: *Proceedings of the ASME Summer Heat Transfer Conference*, Jacksonville, FL, 2008, pp. 645–650.
- [16] G.V. Kuskov, Y.F. Maidanik, Macroscopic boundary angle of wetting of sintered capillary structures of heat pipes, *J. Eng. Phys.* 50 (1) (1986) 53–58.
- [17] B.D. Iverson, S.V. Garimella, Experimental measurements of heat and mass transport in heat pipe wicks, in: *Proceedings of the ASME Heat Transfer/Fluids Engineering Summer Conference*, Charlotte, NC, 2004, pp. 209–217.
- [18] K.K. Brown, H.W. Coleman, Estimating uncertainty intervals for linear regression, in: *Proceedings of the 33rd Aerospace Science Meeting and Exhibit*, Reno, NV, 1995.
- [19] A. Faghri, *Heat Pipe Science and Technology*, Taylor & Francis, Washington, DC, 1995, pp. 123–138.
- [20] J.K. Carson, S.J. Lovatt, D.J. Tanner, A.C. Cleland, Thermal conductivity bounds for isotropic, porous materials, *Int. J. Heat Mass Transfer* 48 (11) (2005) 2150–2158.